applied sciences

MDPI

Article

Additive Manufacturing of Glass-Ceramic Parts from Recycled Glass Using a Novel Selective Powder Deposition Process

João Vasconcelos [1], Manuel Sardinha [2], Carlos M. S. Vicente [2] and Luís Reis [1,2,*]

[1] IST—Instituto Superior Técnico, University of Lisbon, 1049-001 Lisbon, Portugal
[2] IDMEC—Instituto de Engenharia Mecânica, Técnico Lisboa, University of Lisbon, 1049-001 Lisbon, Portugal
* Correspondence: luis.g.reis@tecnico.ulisboa.pt

Abstract: Additive manufacturing technologies have been in continuous growth due to their advantages over traditional manufacturing. The iro3d is a powder deposition machine designed to build metal parts. This research work proposed the adaptation of the iro3d selective powder deposition process to allow the production of glass-ceramic parts using recycled glass powders. Various specimens were produced using different deposition strategies such as build orientation and sintering holding times. Specimens were evaluated in terms of geometric distortions (shrinking and warping) and in terms of mechanical performance (flexural behavior and hardness). Two geometrically complex test parts were also produced to infer the minimum feature size capabilities of the process. The results denoted parts that displayed significant geometrical deviations, which could be correlated with some of the tested parameters. Through the addition of sand to the tested specimens, we demonstrated that distortions could be mitigated with proper control of the powder's coalescence. In the end, the specimens' fracture surfaces were examined, and the presence of porosities was correlated with their mechanical properties. The results demonstrated that the iro3d SPD process could be used to produce additively manufactured glass parts.

Keywords: iro3d; sintering; build orientation; sand; shrinkage

Citation: Vasconcelos, J.; Sardinha, M.; Vicente, C.M.S.; Reis, L. Additive Manufacturing of Glass-Ceramic Parts from Recycled Glass Using a Novel Selective Powder Deposition Process. *Appl. Sci.* **2022**, *12*, 13022. https://doi.org/10.3390/app122413022

Academic Editor: Abílio Manuel Pinho de Jesus

Received: 30 November 2022
Accepted: 15 December 2022
Published: 19 December 2022

1. Introduction

Additive manufacturing (AM) enables the production of geometrically complex structures with, potentially, enhanced mechanical performance, often allowing savings in costs and process time. Components are usually produced based on a digital model by adding material in a layer-by-layer manner. One of the main advantages of AM is its ability to fabricate parts with complex geometries, which are very difficult to obtain with traditional production techniques [1,2].

Metal and ceramic AM machines, and associated production costs, are commonly higher when compared with other AM technologies, partially because powders are difficult to process [3,4]. The use of glass covers many fields, some of which are indispensable to our current lives. Glass and other ceramic materials share most of the difficulties of printing with metals. Their durability, optical characteristics, and unique mechanical properties are examples of what promotes the interest in the 3D printing of these materials. Moreover, due to their brittleness, obtaining geometrically complex ceramic parts with conventional subtractive technologies is often very difficult or not possible at all [5]. The 3D printing of glass is still far from reaching the development stage of polymers or metals. Currently, reports of additively manufactured glass parts can be found for applications such as ornaments, optical elements, or components for microfluidics, in fields such as biology, chemistry, and medicine [6–9]. Concerning the 3D printing of glass, both material extrusion and powder bed fusion processes have been employed, with the main problems identified related to temperature control and a grainy layered outcome, respectively [10–12]. Glass has also been successfully printed by vat photopolymerization, using both stereolithography

and digital light processing techniques. In some cases, specially prepared resins are used, and the layered curing process remains the main issue [13,14].

In 2019, with the introduction of low-cost 3D printers such as the iro3d, the AM of these materials became closer to becoming more economically viable and competitive. The iro3d is a low-cost 3D printer based on a selective powder deposition (SPD) process, designed to print metal parts [15]. The research by Magalhães et al. [16] validates the SPD process through the production of tin bronze specimens and details several relevant aspects of the manufacturing technique requirements. Nonetheless, reports on its characteristics and applicability are still scarce, which justifies the need to study its processing capabilities. The validation of SPD can help the technology to become more relevant, economically viable, and competitive. For this reason, this work focused on investigating the potential of the iro3d and its SPD process to produce glass parts.

Initially developed to produce metal parts, the iro3d (Figure 1A) has the potential to be material agnostic if powders fulfil the necessary process requirements. Naturally, powder morphology varies according to the manufacturing process used to produce its particles [17], impacting powder packing density [18] and therefore the mechanical properties of components. Particle shape will also affect flowability and packing, with spherical particles being preferred over irregularly shaped ones [19]. In the deposition of powders, flowability is essential to achieve homogeneity among the layers of the build [20]. Powder flowability can be enhanced with coarser spherical particles, low moisture content, and a narrower particle size distribution (PSD) [21,22]. Even though coarser particles can be associated with better flowability, a wider, bimodal PSD type results in a faster flowing of the powder particles, improving the packing density [23]. Furthermore, a narrow PSD with a high void ratio will increase the permeability in the horizontal directions, and a higher mean diameter of the powder particles increases the vertical permeability [24]. For the iro3d SPD, better flowability should be prioritized [25], taking into consideration that powders' chemical compositions will greatly affect the printed parts [26]. Regarding the chemical properties of the support powder, both regular sand and silica sand can be used as the support material. Both sand types have melting points above 1500 °C, which is higher than the reported values for glass sintering that start at around 650 °C [27]. Even so, 5% to 20% of regular or brown sand are impurities such as iron, carbonate, and potassium, which make some sand types chemically reactive, possibly damaging the crucible or glass when fired up.

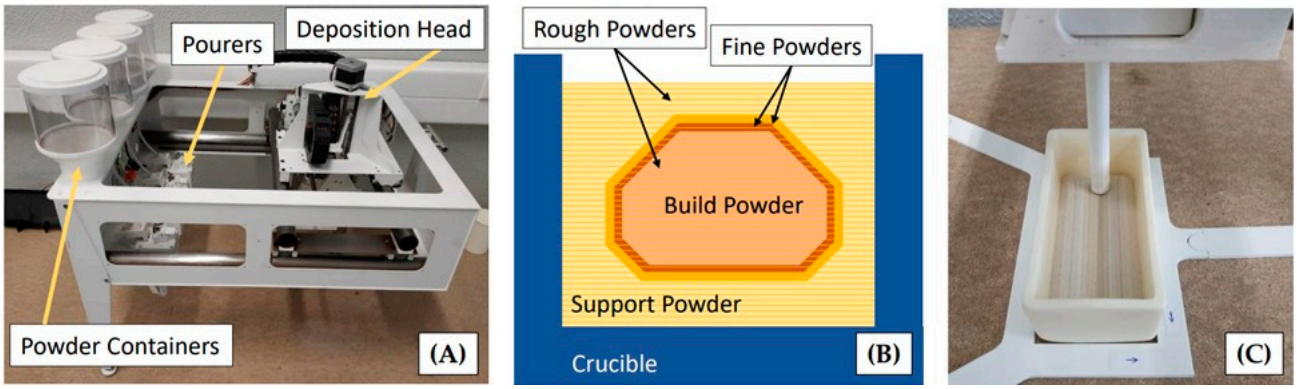

Figure 1. The iro3d selective powder deposition (SPD) process. (**A**) Iro3d model C machine with main components identified. (**B**) Section view scheme of the crucible with support and build powders inside, after the deposition stage and before sintering. (**C**) Example of a pourer depositing glass powders inside an alumina crucible.

To produce metal parts with the iro3d, a powder runner is usually built on top of the part. Inside the furnace, this runner allows the infill metal to flow through it, soaking the remaining metal powder once the infill material melting temperature is achieved [16].

Concerning glass powders, the manufacturing workflow used to produce specimens in this research did not include the building of a runner during deposition or the use of infill material in the sintering stage. The scheme of Figure 1B demonstrates the result of a build, after the layer-by-layer process of selectively pouring glass and support powders into a crucible. Figure 1C is meant to demonstrate the deposition stage where, within each layer, the head system exchanged its tooltip between the four available pourers.

During the powder deposition stage of the iro3d, the particles are distinguished by their mean diameters, being divided into two different categories, fine and rough sizes. Fine powders were employed in the border between build and support materials, as exemplified in the scheme of Figure 1B, promoting the reduction of surface roughness. Considering the pourer's diameter, the build and support powders' PSDs should be roughly 1/10 of the pourer diameter, between 40–90 µm and 90–190 µm for fine and rough powders, respectively [16], which is in line with the work performed by D. Schulze [28] that recommends powders to be five to 10 times smaller than the given outlet diameter.

Regarding the iro3d SPD classification within AM process families [29], the two closest standardized AM categories are powder bed fusion and binder jetting [30]. Even so, SPD does not use a binder in each deposited layer of powders, and its temperature inside the furnace does not reach the melting temperature of the build powder [31]. For this reason, SPD could be better defined as a bottom-up layered technique that selectively deposits small discrete particles using a single channel [32], or be understood as an indirect powder bed process that uses a thermal source as a post-processing stage to cast or sinter the final part [33].

This research aimed to evaluate the adequacy of the iro3d SPD process in the production of glass-based products. To do so, several cuboid specimens were produced under variable powder deposition and sintering strategies.

Several studies have focused on evaluating glass sintering stages, namely, the effect of powder composition and the temperatures involved. Yong-Taeg et al. [34] used high-purity silica powder mixed with impurities and found that transparent glass could be obtained in a high-vacuum atmosphere above 1400 °C. Using a silica sand-based material, the work by Yang et al. [35] concluded that increasing sintering temperatures from 640 °C up to 680 °C would promote shrinkage and lower porosity. Experiments with recycled glass from windshield waste conducted by Gualberto et al. [36] noted the difference in parts made with recycled glass and recycled glass with niobium oxide.

In this work, the effects of process variables such as build orientation, build material, sintering temperature, and thermal cycle time on the geometrical distortions (shrinking and warping) and mechanical performance (microhardness and transverse rupture strength) were analyzed. In addition, a preliminary study on the capabilities and limits of the technology was carried out using two test parts composed of various feature sizes.

2. Materials and Methods

Even if the iro3d SPD process is simplified when producing glass parts instead of metal ones, production should consider the importance of crucibles, powders, or furnace in the behavior and structural integrity of parts.

2.1. Iro3d Machine, Furnace, Crucibles, and Specimens

The iro3d machine used in this study was a model C (Figure 1), with an available build volume of roughly (279 × 274 × 110) mm^3. This model was equipped with two fine and two rough pourers. The main difference between them was the outlet diameter, which took the values of 1.9 mm for both rough pourers, 1.17 mm for the fine build powder, and 0.9 mm for the fine support powder.

The thermal source used during the sintering stage was the Termolab (Águeda, Portugal) MLM 12/12 with the Eurotherm (Worthing, UK) programmable controller EPC3016. Parts were sintered in an oxygen-rich atmosphere.

The crucibles used were composed of alumina (99% Al_2O_3) and were either cylindrical or parallelepiped in shape. According to their manufacturer, they had a linear expansion coefficient of $7.8 \times 10^{-6}\ ^{\circ}C^{-1}$ and a thermal conductivity of 25 W/m·K.

Test specimens used in this study were cuboids measuring 85 × 15 × 5 mm and were designed following the ASTM standard C158-02—Test Methods for Strength of Glass by Flexure (Determination of Modulus of Rupture) [37]. In a preliminary study, similar but thinner cuboid specimens' dimensions were also used to grasp a better understanding of the process. Figure 2A shows the positioning of specimens inside the two types of crucibles used.

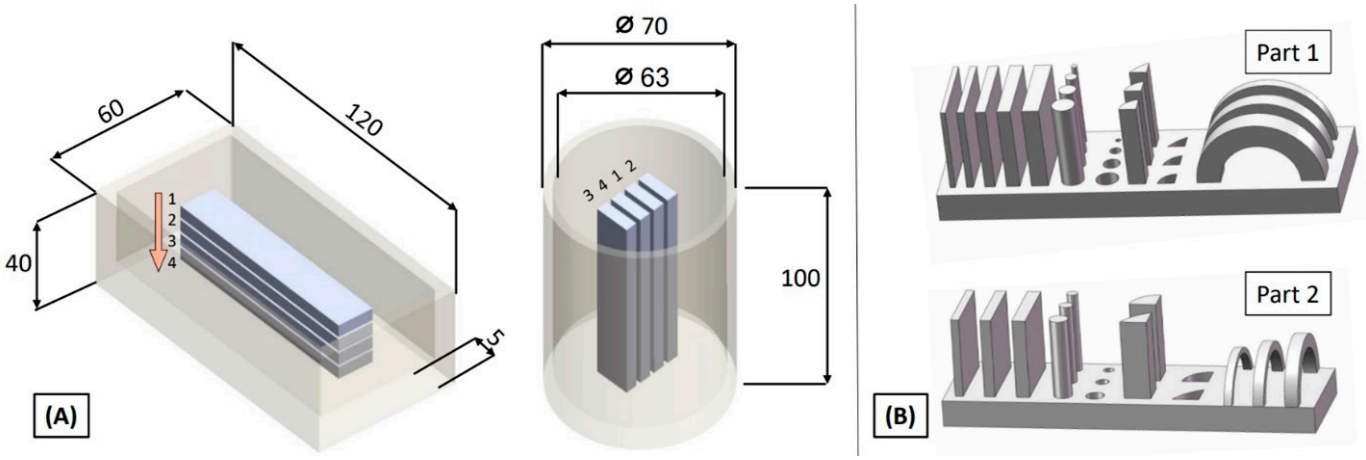

Figure 2. Overview of produced parts. (**A**) Scheme of the positioning of specimens inside the two types of crucibles. The numbering sequence is defined for the position of each specimen within a batch. Horizontally built specimens in parallelepiped crucibles (on the left) and vertically built specimens in cylindrical crucibles (on the right), where dimensions are in mm. (**B**) Test parts produced.

Figure 2B shows two different test parts designed to better understand the limitations of the iro3d SPD process. These parts are composed of small features such as holes, pillars, and walls whose objective was to guide the design for AM of glass parts produced with SPD. Detailed information on their features size can be consulted in [25]. This was a preliminary study that aimed to complement the one represented in Figure 1A, by providing notions on the production capabilities of features such as minimum thicknesses, hole diameters, and overhangs.

2.2. Build and Support Powders

Two different glass build powders were kindly provided by two Portuguese companies, Blasqem (Maia, Portugal) and Coniex (Maia, Portugal). They were composed of glass microspheres, and their morphology was analyzed in a SEM session using the model Phenom Pro G6 from Thermo Fisher Scientific (Waltham, MA, USA). The results of this analysis can be seen in Figures 3 and 4.

The glass from Blasqem was used as the build powder to produce the cuboid specimens. The glass microspheres that composed it were fused from soda-lime glass that was recovered from the glass of broken windows. Afterward, they went through a sieving process to achieve PSDs between {42–122} µm and {122–174} µm. The glass from Coniex was used as the build powder to produce the test parts in Figure 2B, and a few thin specimens were used in preliminary studies. Coniex glass microspheres were also recovered from shredded window glass, which suffered a cleaning process that removed impurities before it was then taken to a dedicated furnace. They were provided with PSDs between {70–110} µm and {100–200} µm.

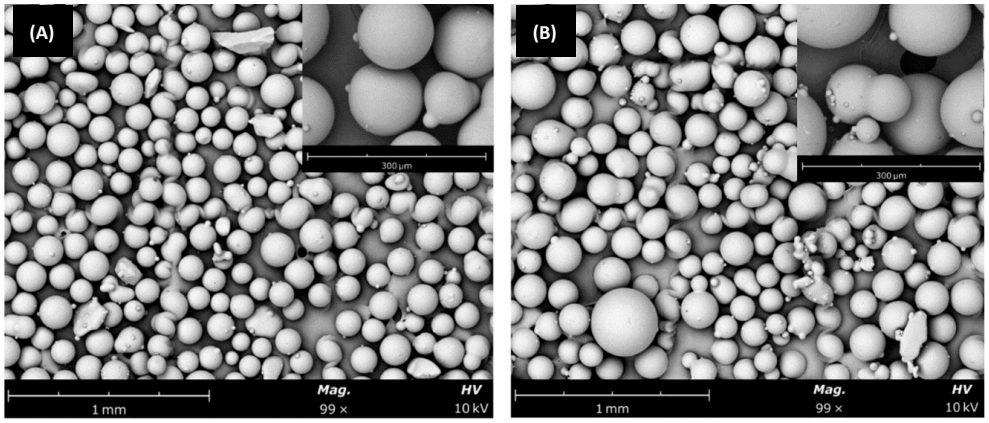

Figure 3. SEM image of the Blasqem glass build powder. (**A**) Fine, and (**B**) rough.

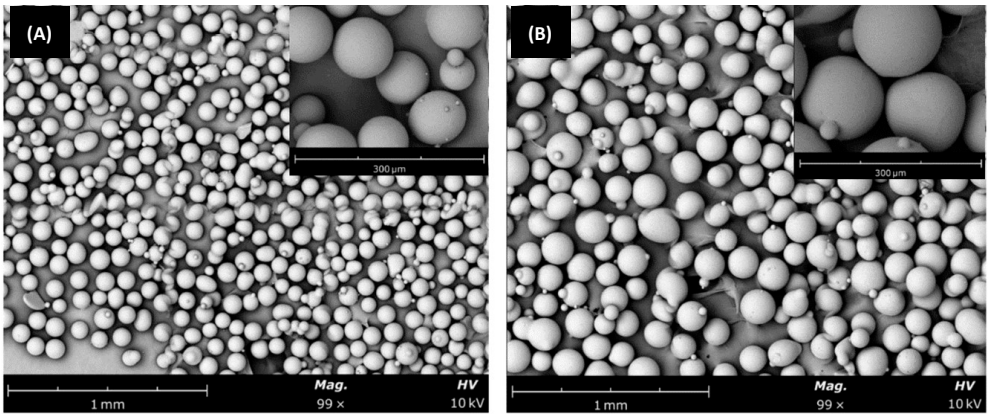

Figure 4. SEM images of the Coniex glass build powder. (**A**) Fine, and (**B**) rough.

The compositions and properties of these powders are detailed in Table 1.

Table 1. Glass powder composition and properties. Data compiled from [30,38,39].

		Blasqem	Coniex
PSD (µm)	Fine Rough	42–122 122–174	70–110 100–200
Hardness (Mohs)		6	6
Solid Density (g/cm^3)		2.5	2.5
Apparent Density (g/cm^3)	Fine Rough	1.41 1.46	1.38 1.38
Flowability (mg/s)	Fine Rough	66 246	74 257
Melting Point (°C)		{700–850}	~730

The fine support powder that was used was composed of sand from Atomwell® (Dayton, TX, USA) and had a PSD of {74–100} µm, and the rough powder was from Strobel Quarzsand GmbH (Freihung, Germany), having a PSD of {122–174} µm. Both support materials had a reported melting point of over 1500 °C.

2.3. Experimental Procedure

The production of specimens within this research can be divided into three distinct stages and groups of samples. First, the preliminary study concentrated on identifying process intricacies and choosing the sintering temperature of the specimens. Second, the main study, where specimens were produced under constant conditions (except for the variable under study), was the focus of the results of this work. Finally, the third study

consisted of the production of the two test parts with geometrically complex details, which allowed the assessment of process limitations.

Each batch of produced specimens was evaluated in terms of geometrical deviation from the theoretical dimensions of the CAD model (warpage and shrinkage), and its mechanical resistance was estimated through three-point bending and microhardness tests. To complement, the weight of the specimens (and powders) was measured using the laboratory precision scale KERN PCB.

2.3.1. Preliminary Study

In a preliminary study, batches of thin cuboid specimens were produced in the parallelepiped crucibles and were sintered at temperatures of 750, 800, and 850 °C, with a sintering hold time of 1 h. The Coniex glass microspheres' sintering temperature was estimated at 730 °C by the material provider. Nevertheless, the work by Jaafar et al. [40], which treated a similar type of soda-lime-silica glass with sintering temperatures between 700 and 1000 °C, could be consulted for alternatives.

These specimens were evaluated in terms of geometrical distortions and transverse rupture strength, but since their size was not equal to the test samples of the main studies that followed, the quantitative results of this analysis were only used as a decision base for the subsequent work. With no visible relation to the sintering temperature, specimens revealed significant levels of geometrical distortions. To assess the possible source of such distortions, a research hypothesis for the subsequent study was created using sand as the build material. Notably, the distortions observed in the samples of the preliminary study induced a significant error during the strength evaluation. For this reason, the main study used 85 × 15 × 5 mm cuboid specimens, the ones shown in Figure 2.

2.3.2. Main Study: Sintering Time, Sand Percentage, and Position Inside the Crucible

In the main study of this research, a total of 14 batches with four prismatic specimens were produced, with each batch representing a process parameter under study. Specimens were printed in both rectangular and cylindrical crucibles, which implied different build directions, horizontal and vertical, respectively. Note that the effect of the position of each specimen in the crucible was also a variable under study, namely, in the horizontally built specimens, since the weight on top of specimens and lateral clearance could influence the sintering stage.

In the first eight batches, glass microspheres were used as the build powder, and the hold time of a sintering temperature of 750 °C was tested, with values varying between 1, 2.5, 4, and 8 h. In the remaining six batches, specimens were produced at a sintering temperature of 750 °C and a hold time of 1 h. The build powder of these six batches had not only glass but a percentage of sand mixed with it, varying between the values of 20%, 40%, and 60% in weight.

To identify each batch of specimens, a labelling system consisting of a number or percentage value and one letter is detailed in Table 2. The letter is related to the primary study variable, i.e., the orientation of the specimens. The letter "h" represents horizontally printed specimens, and the letter "v" represents vertically printed specimens. The number or percentage was related to a secondary study variable, i.e., hold time (Δ_{hold}) or sand percentage in weight ($\%_{sand}$).

To assess the relative shrinkage of produced parts, all three dimensions of each specimen (length, width, and thickness) were measured using a digital caliper, in three different sections along the specimen's length. The locations of these sections were maintained throughout measurements, i.e., always on the same level of altitude in vertical specimens or longitude in horizontal specimens. The volume of the prismatic specimens was computed using the average of all measurements taken in each specimen, and a ratio between theoretical and experimental volume values was used to compute shrinkage. Warpage was evaluated mostly from a visual and qualitative perspective.

Table 2. Labelling of each batch of four specimens according to each study variable.

Label	Hold Time [Hours]	Sand Percentage	Build Orientation
1h	1	0	Horizontal
1v	1	0	Vertical
2.5h	2.5	0	Horizontal
2.5v	2.5	0	Vertical
4h	4	0	Horizontal
4v	4	0	Vertical
8h	8	0	Horizontal
8v	8	0	Vertical
20%h	1	20	Horizontal
20%v	1	20	Vertical
40%h	1	40	Horizontal
40%v	1	40	Vertical
60%h	1	60	Horizontal
60%v	1	60	Vertical

The flexural property assessment was conducted on a Universal Testing Machine Instron 5566 with a 500 N load cell and a crosshead speed of 1 mm/min. The transverse rupture strength (σ_{TRS}), flexural strain at rupture (ε_r), and modulus of elasticity in bending (E_{Bend}) were computed using Equations (1)–(3).

$$\sigma_{TRS} = \frac{3P_r a}{2bt^2} \text{ [MPa]} \quad (1)$$

$$\varepsilon_r = \frac{6\delta_r t}{a^2} \quad (2)$$

$$E_{Bend} = \frac{a^3 k}{4bt^3} \times 10^{-3} \text{ [GPa]} \quad (3)$$

where P_r is the breaking load; a is the distance between supports, the span (44 mm); and t and b are the experimentally measured values of thickness and width, respectively. In Equation (3), k is the flexural stiffness, which is the initial slope of the load deflection curve, obtained with the graphical method.

After the flexural tests, four vertically printed specimens, one for each sintering holding time, and two horizontally printed specimens, with two different hold times, were selected for the microhardness tests. Hardness Vickers (HV) was measured using a Shimadzu HMV-2 digital microhardness testing machine. In each specimen, four measurements were performed, two in each broken piece of the specimen, distanced 15 and 30 mm from the two edges, as seen in Figure 5.

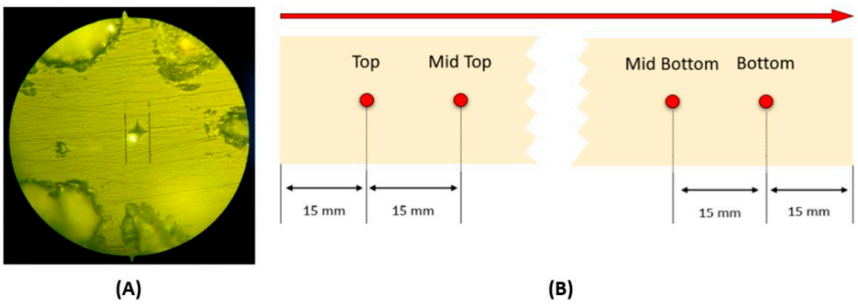

Figure 5. Microhardness test procedure. (**A**) Example of Vickers indentation on a specimen. (**B**) Location of hardness measurements.

2.3.3. Test Part Production Study

In the third study type, the production of two test parts with geometric details aimed to provide a better understanding of production limitations. The test parts contained walls with different thicknesses, circular columns, holes, arc-shaped columns and holes, and semi-circular bridges with square sections. These details were an attempt to define a reference for minimum thicknesses, hole sizes, overhang angles, and slenderness of external bodies.

3. Results and Discussion

The production process of glass-ceramic test specimens and parts using the iro3d was confirmed to be simpler when compared with the production of parts that required the use of infill material, such as metal parts production [16]. Furthermore, by not having to produce a runner on top of the part during the deposition stage, the production time of each part was significantly reduced. Even so, due to the brittle behavior that the produced parts displayed, measurements and support powder removal were delicate and time-consuming tasks.

3.1. Preliminary Study Results

When varying the sintering temperatures (T_{sint}), no clear linear dependency with distortions was found, which contradicted what D. Yang et al. [35] concluded using borosilicate glass and temperatures between 640 °C and 680 °C. However, when compared with research results using recycled soda-lime-silica glass from windshields, as presented in Gualberto et al. [36], or with recycled sauce bottles in Jaafar et al. [40], similarities could be found. Namely, the specimens sintered at 800 °C had the smallest shrinkage. Gualberto et al. found that increasing the sintering temperature up to 800 °C would lower the density of the specimens since the crystallization would occur before the sintering was complete, causing a rapid increase in viscosity and successively less dense materials [36]. Jaafar et al. [40] state that a further increase in the sintering temperature to values above 800 °C, together with secondary effects, would lower the viscosity of the glass and provoke the increase in density, which can result in greater shrinkage. However, these comparisons are limited in the sense that the materials used, processing techniques, and sintering conditions are different from the ones used in this study. Furthermore, in the iro3d SPD, the parts were sintered inside the crucible and involved sand, which affected the heating, cooling, and crystallization processes. Due to their very thin sections, the shrinkage of these specimens was relatively small, with the greatest mean values being for the specimens sintered at 850 °C. All specimens displayed a brittle fracture with a very short displacement at break. The average transverse rupture strength (σ_{TRS}) of these tests was below the reported values. An explanation could be the existence of additional stress concentrations from warping along the length axis, possibly due to uneven shrinkage. The smallest shrinkage was observed in the specimens sintered at 750 °C.

Considering the distortions observed, the hypothesis of mixing sand with glass and using the mixture as build powder was tested to infer sand's influence on shrinkage.

3.2. Geometric Distortions and Warpage

Concerning the main tests of this research, both horizontally and vertically built specimens displayed a visible amount of shrinkage. Generally, the shrinking was more pronounced in dimensions that were aligned with the vertical direction of the build, meaning a significant impact on the thickness of horizontally printed specimens and the length of vertically printed specimens. Shrinkages up to 22.93% and 16.62% were verified in thickness and length, respectively. In addition, horizontally built specimens presented a defined warpage tendency, with specimens that were closer to the top/open surface of the crucible displaying higher warping values. The bottom specimens shrank but displayed little warping. One explanation for this could be the fact that each specimen was subject to a different weight load on top of it. Another effect was that during shrinking, the support sand above a specimen flowed downwards, and the glass microspheres in the surroundings were affected by this flow of powders. This effect was accumulated in some areas of the

crucible, and the displacement of the center glass powders became larger as the number of specimens below the specimen under consideration increased, promoting warping.

This influence of build orientation on warping can be observed in Figure 6A,B, which show batches 8h and 8v. The influence of the sand percentage in the reduction of warping is also clear in Figure 6C.

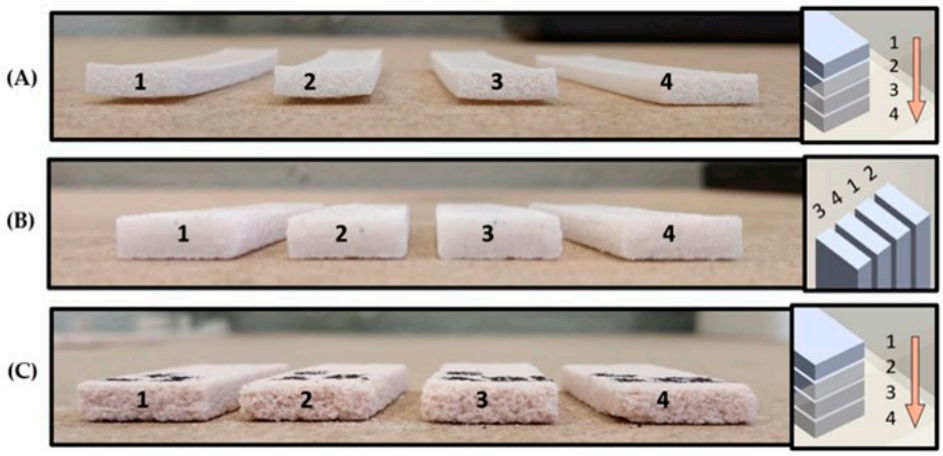

Figure 6. Representative example batches of specimens and their relative positions inside the crucible. (**A**) Horizontal specimens. (**B**) Vertical specimens. (**C**) Horizontal specimens with 60% sand in weight.

Regarding the holding time (Δ_{hold}) analysis in [35], in Figure 7A, in the horizontal specimens, the shrinkage variations were not very significative, being the maximum mean shrinkage value obtained in the thickness (15.7%), for a Δ_{hold} of 8 h. In vertically printed specimens (Figure 7B), a Δ_{hold} of 1 h resulted in the shorter specimens, while the longer specimens were obtained for a Δ_{hold} of 8 h. Considerable variations on the average shrinkages were detected for the width (4%) and thickness (7.61%), possibly due to problems inherent to the printing process. The most notable shrinkages happened, as expected, in the vertical directions, i.e., along the thickness of horizontally built specimens and along the length of vertically built specimens.

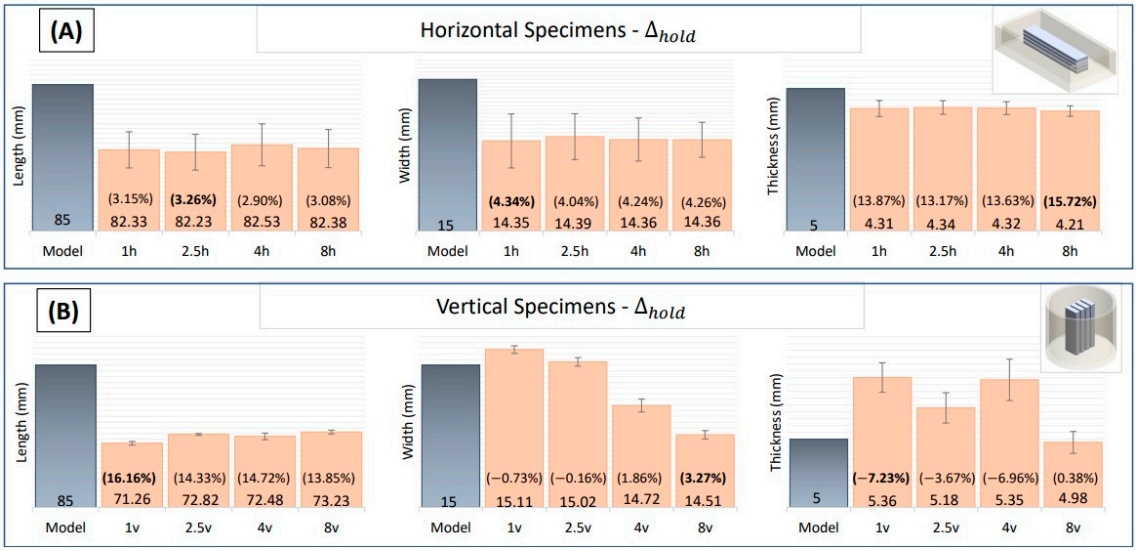

Figure 7. Average geometric distortion (shrinkage) of specimens under variable sintering hold time (Δ_{hold}). (**A**) Horizontally built specimens. (**B**) Vertically built specimens. Absolute values of each measure are in mm, and relative variation from CAD model is a percentage. Negative values indicate an increase in size.

Concerning the influence of sand percentage ($\%_{sand}$) on horizontal specimens' geometrical distortions, the shrinkage was indeed reduced to nearly zero, as intended, in specimens with sand percentages over 40% (Figure 8). It can also be seen that the standard deviations that were very pronounced in some cases were minimized, possibly because the glass microspheres were now limited by the sand particles and could not flow. The same happened in the vertical specimens, as the specimens with 60% sand even expanded (length shrinkage of −0.77%), which was possible considering that the apparent density of the glass microspheres was superior to the apparent density of the sand used as support powder.

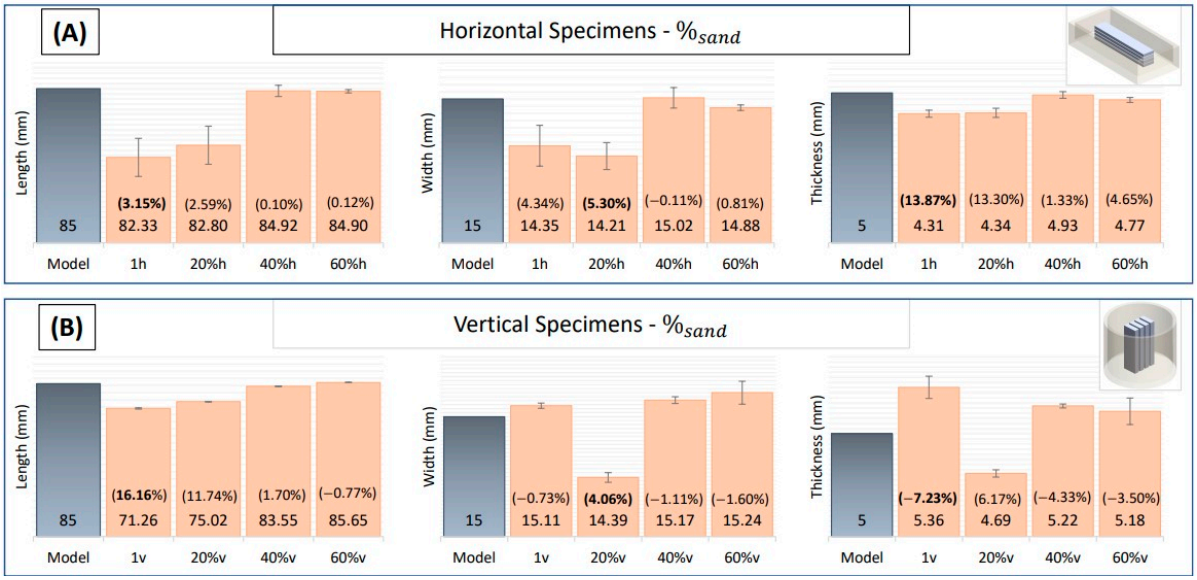

Figure 8. Average geometric distortion (shrinkage) of specimens with different sand percentage ($\%_{sand}$). (**A**) Horizontally built specimens. (**B**) Vertically built specimens. Absolute values of each measure are in mm, and relative variation from CAD model is in percentage. Negative values indicate an increase in size. (Batches 1h and 1v are present in the graphs for comparison, as they contain specimens subject to the same sintering temperature and hold time but had 0% sand mixed in the build powder.)

Even though they were printed horizontally, the specimens of batch 60%h, printed with 60% sand mixed in the build powder, did not warp. When measuring dimensions along the length of each vertically printed specimen, the width and thickness decreased, from the base of the crucible/specimen to the top.

Naturally, the sand percentage had an impact on the mass, volume, and density. As the sand percentage increased, the glass microspheres were stopped from shrinking and flowing. Since sand was lighter and less dense than glass, the mass of the specimens decreased, their volume increased as sand stopped the glass powder from shrinking, and the density consequently decreased. From 0% to 60% sand, the average mass of the specimens decreased 20%, from 10–11 g to 8–9 g, and the density decreased roughly 30–35% from 2 g/cm^3 to 1.3–1.4 g/cm^3.

It should be noted that independent of sintering temperature and hold time, in the printing process of vertical specimens, powders were poured in smaller areas, at a higher deposition pace. Contrary to what happened in horizontally built specimens, vertical builds almost always used only fine-sized powders. The frequent starting and stopping of the pouring could result in extra glass powder being poured into each layer due to the closing of the pourers not being ideal. On average, vertical specimens tended to be heavier and larger than horizontal ones, their mass varied from 9–10 g to 11–12 g, and the volume was from around 5000 mm^3 to around 5700 mm^3.

3.3. Flexural Properties

Naturally, the glass-ceramic specimens produced behaved as brittle materials. The stress–strain curves of batch 8v are represented in Figure 9. These were a representative example of flexural tests after load deflection curves were translated into stress–strain using the measured average dimensions of each specimen's transverse section. The remaining experimental data can be found in the Supplementary Materials associated with this research.

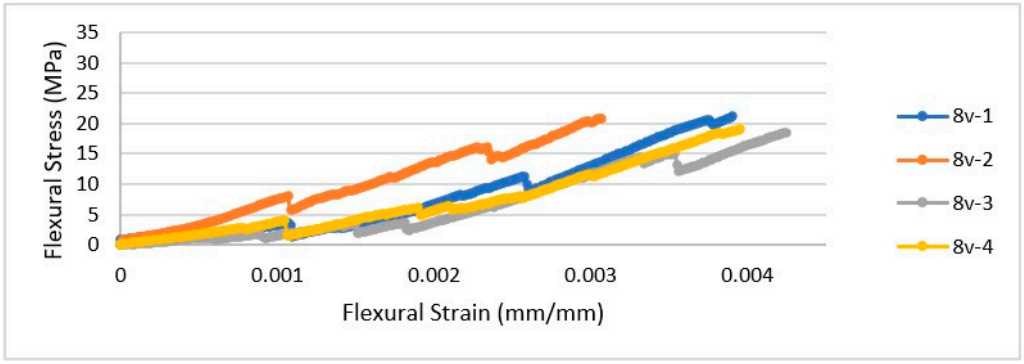

Figure 9. Flexural stress–strain curves of the specimens of batch 8v.

To globally analyze the impact of the process parameters in the behavior of SPD specimens, a simplification was made, only displaying the average transverse rupture strength (σ_{TRS}) and the average modulus of elasticity in bending (E_{Bend}), noting that in some cases, the rupture strain was very variable. Irregularities such as down-steps happened in all types of specimens. These down-steps corresponded to times at which sections partially broke. These down-step-shaped irregularities are not rare in stress–strain graphs obtained in bending tests with similar materials. One likely primary source of error in the flexural assessments was related to the visual warping of each specimen. Considering this average of σ_{TRS} and E_{Bend} between batches, Figure 10 illustrates the global results obtained in the bending tests.

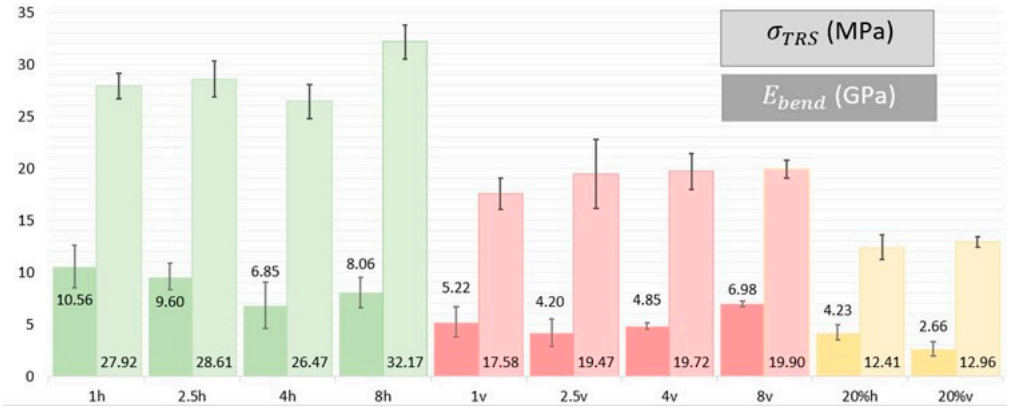

Figure 10. Average transverse rupture strength (σ_{TRS}) and modulus of elasticity in bending (E_{Bend}). Darker bars indicate the average E_{Bend}, and lighter-colored bars indicate the average σ_{TRS}.

When it came to the specimens with 20% sand mixed with the glass, the down-steps became bigger and more frequent. This behavior was predicted and could be related to the fact that the sand particles did not sinter and therefore were merely held together due to the sintered glass microspheres. The sections containing bigger percentages of mixed sand were more susceptible to breaking, making the specimens weaker. Figure 11 shows an example of the fracture surfaces of a pure glass specimen and a specimen with 60% sand.

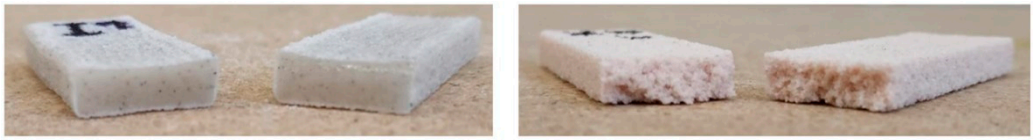

(A) (B)

Figure 11. Example of fractured specimens. (**A**) Horizontally built specimen, with 0% sand, displaying a smooth fracture surface. (**B**) A similar specimen built with 60% sand, displaying a granular and irregular type of fracture surface.

Looking at the specimens printed with 100% glass microspheres, the horizontally printed specimens sustained the higher flexural stresses, from 25 MPa to 33 MPa, while the maximum flexural stress for the vertically printed specimens was below 20 MPa.

Despite undergoing a sintering stage that could minimize the layer effect, the results on build orientation still revealed the natural tendency of layered processes. In the horizontal specimens, the layers were aligned with the bending plane, perpendicularly to the direction of the load. In vertical specimens, layers were colinear with the load direction, which made them more susceptible to breaking. When considering the specimens with 20% sand, the orientation of the specimens did not significantly impact the maximum stress, as both types only sustained flexural stresses up to 13 MPa.

3.4. Microhardness

Microhardness tests were performed in four vertically built specimens (one for each sintering hold time) and two horizontally built ones (with Δ_{hold} of 4 and 8 h). No specimen with mixed sand was tested as they were considered too frail. The results from the microhardness testing in hardness Vickers (*HV*) are summarized in Table 3. These results were aligned with the literature reports that quantified the hardness of this type of glass with values ranging from 540 *HV* to 660 *HV*. No clear tendency was found with the sintering temperature or the altitude of the section of the specimen inside the crucible.

Table 3. Microhardness Vickers results.

	Microhardness Vickers (*HV*)				
Specimen	**Top**	**Mid Top**	**Mid Bottom**	**Bottom**	**Average**
1v	606	526	512	582	556.5
2.5v	598	587	549	600	583.5
4v	690	619	557	547	603.3
8v	476	591	598	601	566.5
1h	571	595	564	564	573.5
8h	527	653	571	558	577.3

3.5. Internal Structure

Figure 12A,B demonstrate the difference in specimens sintered during 1 h and 8 h, where the porosities were partially dissipated when holding time increased. This fact corroborated the obtained bending results, implying that longer hold times could reduce porosities and improve the strength of the sintered parts. Figure 12C shows a vertically built specimen sintered for 8 h that in comparison with the horizontally built one revealed many more porosities. This could be explained by the more irregular pouring process identified in the vertical specimens and was in line with the obtained bending results.

Figure 12D also contains the fracture surface of a specimen with 20% sand where sharp edges can be identified, belonging to the support sand, as the sand particles used were not as spherical. This observation supported the fact that sand significantly weakened the specimen, as the sand particles did not sinter.

To confirm that the visible spheres in Figure 12 were porosities and not unsintered glass microspheres, specimens were analyzed in a SEM session. Figure 13 shows the

fracture surface of specimen 1h where several spherical voids (in black) or semispherical craters can be found, which most probably originated from trapped gas in the sintering stage. These observations were confirmed by SEM images of the remaining specimens.

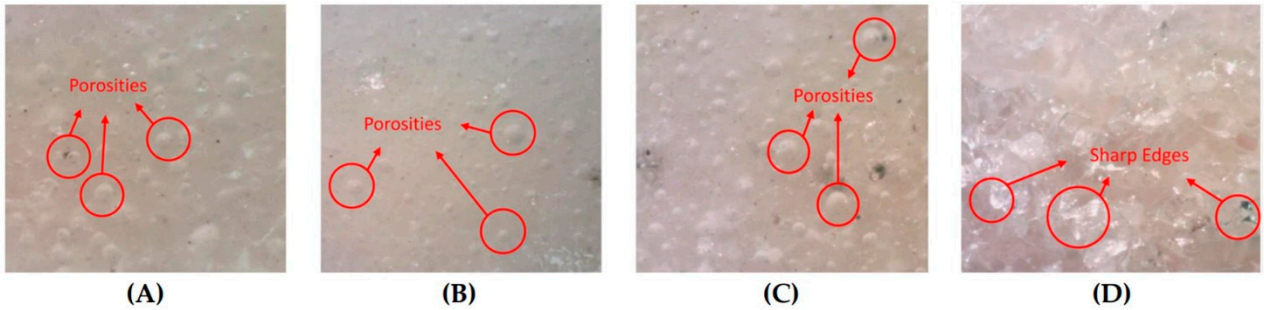

Figure 12. Amplification (∼80×) of the fracture surface of representative specimens. Photos obtained with an AM7025X Dino-Eye eyepiece camera mounted on an Optika SZM trinocular stereo microscope. (**A**) Specimen 1h. (**B**) Specimen 8h. (**C**) Specimen 8v. (**D**) Specimen 20%h.

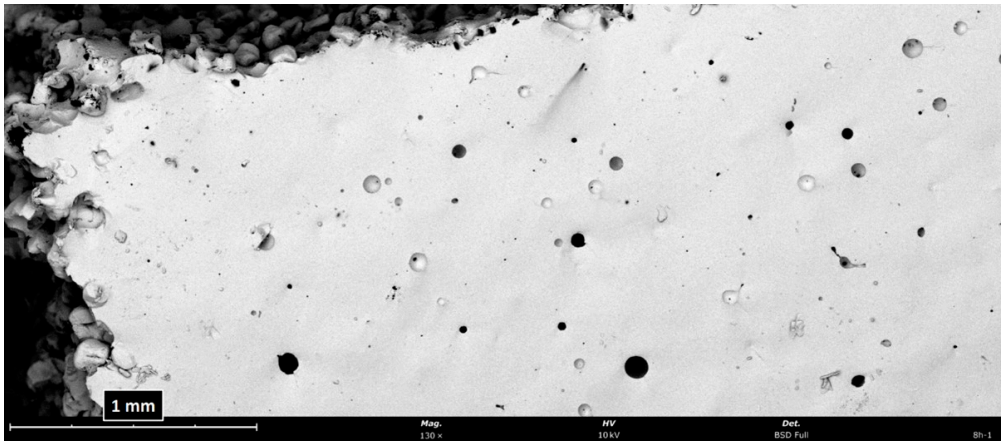

Figure 13. SEM image of the corner of the fracture surface of a specimen from the 1h batch. Image obtained in the desktop SEM Phenom Pro G6 from Thermo Fisher Scientific (Waltham, MA, USA), after samples were coated with gold and palladium.

3.6. Test Parts Inspection

Concerning the test parts produced, out of the five walls of test part 1, only three were printed, i.e., walls with 0.9 and 1.17 mm in thickness (which are the diameters of the openings of the fine and rough pourers) were not visible in the final part, even though their respective build powder was deposited. Notable in both parts, all the walls were thicker on one of the edges, corresponding to the position where the pourer stopped in each layer. The smallest obtained had a width of 1.5 mm, present in test part 2.

Out of the four circular columns and holes, the ones with a 1 mm diameter were not produced, with the minimum circular features having a 2 mm diameter. The arc-shaped details were all printed but were ripped from the part during a cleansing stage. All the semi-circular bridges were printed, with visible distortions. Figure 14 shows the parts after being sintered and cleaned with a metal brush.

As can be seen, the arcs and circles were not well detailed in the final parts. The circular columns in test part 1 were attached, just like the thicker edges of some walls, even though there was a 1.4 mm clearance between them. The bridges were printed in a good semi-circular shape, but their section was very irregular. Furthermore, the small distance between details affected the cylindricity of the circular columns and holes. It was also the increased distance between details that allowed the arc-shaped columns and holes to be "cleaner" in test part 2, making the difference between different radii visible.

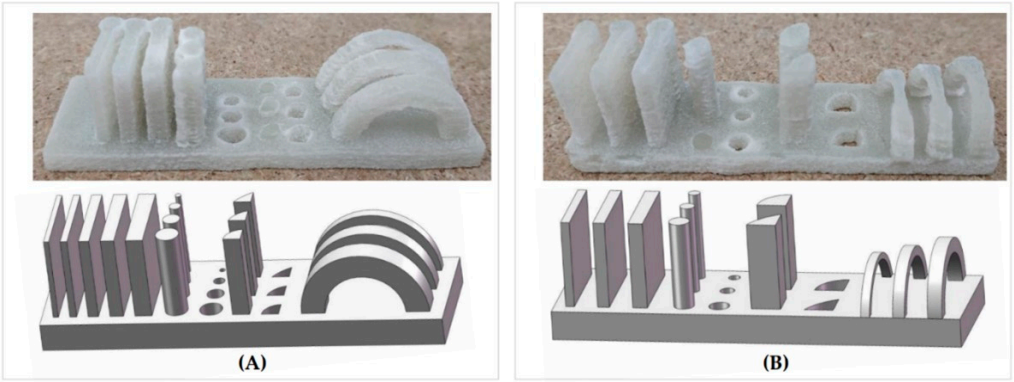

Figure 14. Produced test parts and their comparison with the theoretical CAD model. (**A**) Test part 1. (**B**) Test part 2.

4. Conclusions

In this work, the potential of the iro3d SPD process to produce glass-ceramic parts using glass microspheres obtained from recovered glass waste was investigated through the production of cuboid specimens and two geometrically complex test parts.

A preliminary study was performed to have a clearer vision of adequate sintering conditions, process requirements, and experimental procedure intricacies. These observations led the authors to try to control the distortions of samples by mixing the glass build powders with sand powders (that will not shrink or melt during sintering). Consequently, in this research, the influence of sintering temperature hold time, the sand percentage in the build powder, and specimen position in the crucible were tested. The assessment was complemented with the production of test parts with geometrically complex details, which allowed us to infer process limitations regarding minimum thicknesses, hole sizes, or overhang production capabilities. Overall, specimens were evaluated in terms of geometrical deviation from the theoretical dimensions and subjected to three-point bending and microhardness tests.

The authors conclude that the positioning of parts inside the crucible and, more specifically, the material amount and weight above it significantly influenced the final geometrical accuracy of parts. The higher the horizontal specimens were in the crucibles, the bigger the warpage observed. Neither the temperature nor the hold time had a clear correlation with shrinkage. However, increasing the sand percentage up to 60% reduced the specimen's shrinkage to a minimum. Horizontal specimens with higher sand percentages did not shrink, and no warping was observed. Specimens produced with greater sand percentages were slightly lighter, larger, and less dense due to the lower mass and apparent density of the sand. Additionally, vertical specimens were slightly larger and heavier when compared with horizontal specimens. This could be justified by the fact that in the deposition stage, the build powder was poured much more frequently in the vertical specimens, even though in smaller areas, which resulted in an excess of powder being poured.

Possibly due to an increase in humidity or due to the size and morphology of the powders, their flowing inside the pourers could be interrupted due to clogging, both in the deposition and in the refilling stage. This effect could also be more pronounced in vertical specimens. In the cylindrical crucibles, it could be seen that almost all the build powder used was fine-sized, due to the section area of the specimens. On the other hand, when printing horizontal specimens in the rectangular crucibles, around 25% of the build powder use was fine, and the remaining 75% was rough. This fact had an unknown influence on the comparisons between build orientations, and for this reason, the authors suggest studying the influence of single-size usage of powders.

Overall, increasing sintering hold times resulted in improved mechanical properties, which was corroborated by the smaller number of porosities in the fracture surface of speci-

mens. With a value of 36 MPa, the maximum transverse rupture strength was registered in horizontally built specimens with a sintering time of 8 h. All the specimens of this batch revealed greater strain at rupture when compared with batches sintered for lower hold times. Naturally, vertically printed specimens were generally weaker when compared with horizontally built specimens under the same conditions.

When the sand was mixed with glass as build powder, only percentages up to 20% resulted in specimens presenting brittle behavior as all the other specimens printed with higher percentages of sand were too weak and simply tore apart.

The fracture surfaces of specimens revealed that higher hold times reduced the number of porosities inside the specimens, corroborating the flexural strength results. Vertical specimens presented more porosities when compared with horizontal ones.

To finalize, the printed test parts allow the partial identification of current manufacturing limitations. It can be concluded that to properly design a part to print with the iro3d SPD process, the minimum size of the details needs to be superior to the diameter of the opening of the build pourer. In this work, the smallest printed detail was a wall with a width of 1.5 mm. Also worthy of mention is the fact that the walls were thicker on one of the edges, corresponding to the position where the pourer stopped in each layer. Further studies on the design for AM of the iro3d SPD should be carried out. In the future, aligned with other AM glass applications, geometrically complex glass parts obtained with the iro3d could be incorporated in products such as scaffolds for biomedical applications, ornaments, or electric insulators, if current limitations are overcome.

Even if results denote that manufacturing is still far from reaching its full capabilities, this work proves that the iro3d has the potential to be material agnostic and produce parts using glass and other recycled powders. Naturally, it will be important to evaluate energy usage and efficiency when producing ceramic parts to infer their applicability to end-use parts. For now, quantifying the amount of used energy per part produced is still difficult since it depends on the number of parts produced, their volume and placement inside the crucible, crucible dimensions, and the thermal source used, among others. In addition, the need to have exigent powder parameters such as a spherical shape, a specific particle size, and PSD to promote proper flowability in the pourers might significantly increase the energy consumption and costs of the process. In some cases, if the recovered powder materials, such as glass, require an additional spherization stage, process applicability and sustainability prospects might be partially compromised.

In future work, the authors also suggest developing a mechanism, conceptually similar to the addition of sand, to control the shrinking of parts, without compromising their mechanical resistance. In addition, when evaluating the shrinkage, the use of a single PSD should be tested since fine and rough glass powders can certainly impact the results. Last, by being adequate to process recycled powders, the iro3d might help to promote the circularity of the used materials. In line with this, the authors consider that the assessment of energy consumption, sustainability performance, and cost structure are fundamental future research paths to promote the application of the process in the manufacturing of functional components.

Supplementary Materials: The following supporting information can be downloaded at: https://www.mdpi.com/article/10.3390/app122413022/s1, Figures S1–S10: Stress-Strain Curves of all Batches of specimens.

Author Contributions: Conceptualization, M.S. and L.R.; methodology, M.S. and C.M.S.V.; formal analysis, J.V.; investigation, J.V.; resources, L.R. and C.M.S.V.; writing—original draft preparation, J.V.; writing, M.S.; supervision, L.R. All authors have read and agreed to the published version of the manuscript.

Funding: This work was supported by FCT—Fundação para a Ciência e Tecnologia, through IDMEC, under LAETA, Project UIDB/50022/2020. The authors also gratefully acknowledge the funding of the FCT project, AM-Optical, PTDC/EME-EME/4593/2021.

Institutional Review Board Statement: Not applicable.

Informed Consent Statement: Not applicable.

Data Availability Statement: Not applicable.

Acknowledgments: The authors thank Blasqem, Lda, and Coniex S.A. for kindly providing the glass micro-spheres and Strobel Quarzsand GmbH for kindly providing their sand. Manuel Sardinha gratefully acknowledges FCT, for his PhD research grant reference 2021.04919.BD. This work was supported by FCT—Fundação para a Ciência e Tecnologia, through IDMEC, under LAETA, Project UIDB/50022/2020.

Conflicts of Interest: The authors declare no conflict of interest.

References

1. Picard, M.; Mohanty, A.K.; Misra, M. Recent advances in additive manufacturing of engineering thermoplastics: Challenges and opportunities. *RSC Adv.* **2020**, *10*, 36058–36089. [CrossRef] [PubMed]
2. Gibson, I.; Rosen, D.; Stucker, B. *Additive Manufacturing Technologies: 3D Printing, Rapid Prototyping, and Direct Digital Manufacturing*, 2nd ed.; Springer: Berlin/Heidelberg, Germany, 2014.
3. DebRoy, T.; Wei, H.L.; Zuback, J.S.; Mukherjee, T.; Elmer, J.W.; Milewski, J.O.; Beese, A.M.; Wilson-Heid, A.; De, A.; Zhang, W. Additive manufacturing of metallic components–Process, structure and properties. *Prog. Mater. Sci.* **2018**, *92*, 112–224. [CrossRef]
4. Tofail, S.A.; Koumoulos, E.P.; Bandyopadhyay, A.; Bose, S.; O'Donoghue, L.; Charitidis, C. Additive manufacturing: Scientific and technological challenges, market uptake and opportunities. *Mater. Today* **2018**, *21*, 22–37. [CrossRef]
5. Chen, Z.; Li, Z.; Li, J.; Liu, C.; Lao, C.; Fu, Y.; Liu, C.; Li, Y.; Wang, P.; He, Y. 3D printing of ceramics: A review. *J. Eur. Ceram. Soc.* **2019**, *39*, 661–687. [CrossRef]
6. Zhang, D.; Liu, X.; Qiu, J. 3D printing of glass by additive manufacturing techniques: A review. *Front. Optoelectron.* **2021**, *14*, 263–277. [CrossRef]
7. Dasan, A.; Ożóg, P.; Kraxner, J.; Elsayed, H.; Colusso, E.; Grigolato, L.; Savio, G.; Galusek, D.; Bernardo, E. Up-Cycling of LCD Glass by Additive Manufacturing of Porous Translucent Glass Scaffolds. *Materials* **2021**, *14*, 5083. [CrossRef]
8. Elsayed, H.; Colombo, P.; Crovace, M.C.; Zanotto, E.D.; Bernardo, E. Suitability of Biosilicate®glass-ceramic powder for additive manufacturing of highly porous scaffolds. *Ceram. Int.* **2021**, *47*, 8200–8207. [CrossRef]
9. Elsayed, H.; Zocca, A.; Schmidt, J.; Günster, J.; Colombo, P.; Bernardo, E. Bioactive glass-ceramic scaffolds by additive manufacturing and sinter-crystallization of fine glass powders. *J. Mater. Res.* **2018**, *33*, 1960–1971. [CrossRef]
10. Klein, J.; Stern, M.; Franchin, G.; Kayser, M.; Inamura, C.; Dave, S.; Weaver, J.C.; Houk, P.; Colombo, P.; Yang, M.; et al. Additive Manufacturing of Optically Transparent Glass. *3D Print. Addit. Manuf.* **2015**, *2*, 92–105. [CrossRef]
11. Klocke, F.; Mcclung, A.; Ader, C. Direct Laser Sintering of Borosilicate Glass. In Proceedings of the International Solid Freeform Fabrication Symposium, Austin, TX, USA, 2–4 August 2004; pp. 214–219.
12. Kotz, F.; Plewa, K.; Bauer, W.; Schneider, N.; Keller, N.; Nargang, T.; Helmer, D.; Sachsenheimer, K.; Schäfer, M.; Worgull, M.; et al. Liquid Glass: A Facile Soft Replication Method for Structuring Glass. *Adv. Mater.* **2016**, *28*, 4646–4650. [CrossRef]
13. Moore, D.G.; Barbera, L.; Masania, K.; Studart, A.R. Three-dimensional printing of multicomponent glasses using phase-separating resins. *Nat. Mater.* **2020**, *19*, 212–217. [CrossRef]
14. Kotz, F.; Arnold, K.; Bauer, W.; Schild, D.; Keller, N.; Sachsenheimer, K.; Nargang, T.M.; Richter, C.; Helmer, D.; Rapp, B.E. Three-dimensional printing of transparent fused silica glass. *Nature* **2017**, *544*, 337–339. [CrossRef]
15. Singov, S. 3D Printer. U.S. Patent 20180169956, 21 June 2018.
16. Magalhães, S.; Sardinha, M.; Vicente, C.; Leite, M.; Ribeiro, R.; Vaz, M.; Reis, L. Validation of a low-cost selective powder deposition process through the characterization of tin bronze specimens. *Proc. Inst. Mech. Eng. Part L J. Mater. Des. Appl.* **2021**, *235*, 2681–2691. [CrossRef]
17. Herzog, D.; Seyda, V.; Wycisk, E.; Emmelmann, C. Additive manufacturing of metals. *Acta Mater.* **2016**, *117*, 371–392. [CrossRef]
18. Abu-Lebdeh, T.; Damptey, R.; Lamberti, V.; Hamoush, S. Powder Packing Density and Its Impact on SLM-Based Additive Manufacturing. In *Minerals, Metals and Materials Series*; Springer: Berlin/Heidelberg, Germany, 2019; pp. 355–367. [CrossRef]
19. Dawes, J.; Bowerman, R.; Trepleton, R. *Introduction to the Additive Manufacturing Powder Metallurgy Supply Chain*; Johnson Matthey Technology Review; Johnson Matthey Public Limited Company: London, UK, 2015; Volume 59, pp. 243–256. [CrossRef]
20. Zou, R.; Yu, A. Evaluation of the packing characteristics of mono-sized non-spherical particles. *Powder Technol.* **1996**, *88*, 71–79. [CrossRef]
21. Brika, S.E.; Letenneur, M.; Dion, C.A.; Brailovski, V. Influence of particle morphology and size distribution on the powder flowability and laser powder bed fusion manufacturability of Ti-6Al-4V alloy. *Addit. Manuf.* **2019**, *31*, 100929. [CrossRef]
22. Lu, K.; Hiser, M.; Wu, W. Effect of particle size on three dimensional printed mesh structures. *Powder Technol.* **2009**, *192*, 178–183. [CrossRef]
23. Sun, C.; Tian, X.; Wang, L.; Liu, Y.; Wirth, C.M.; Günster, J.; Li, D.; Jin, Z. Effect of particle size gradation on the performance of glass-ceramic 3D printing process. *Ceram. Int.* **2017**, *43*, 578–584. [CrossRef]
24. Miyanaji, H. Binder Jetting Additive Manufacturing Process Fundamentals and the Resultant Influences on Part Quality. Ph.D. Thesis, University of Louisville, Louisville, KY, USA, 2018. [CrossRef]

25. Santos Vasconcelos, J.N. iro3d—Selective Powder Deposition Influence of Process Parameters in the Mechanical Properties of Glass Specimens Produced by Selective Powder Deposition. Master's Thesis, Instituto Superior Técnico, Lisboa, Portugal, 25 November 2021.
26. Thornton, A.; Saad, J.; Clayton, J. Measuring the critical attributes of AM powders. *Met. Powder Rep.* **2019**, *74*, 314–319. [CrossRef]
27. Jankus, S.M.; Bendikienė, R. Effect of powder type and particles size on microstructure of selective laser sintered parts. *Key Eng. Mater.* **2019**, *799*, 252–256.
28. Schulze, D. *Powders and Bulk Solids: Behavior, Characterization, Storage and Flow*; Springer: Berlin/Heidelberg, Germany, 2008. [CrossRef]
29. *ASTM F2992-12*; Standard Terminology for Additive Manufacturing Technologies. ASTM: West Conshohocken, PA, USA, 2012.
30. Videira Magalhães, S. Selective Powder Deposition Establishment of Process Requirements and Validation through the Production and Testing of Specimens. Master's Thesis, Instituto Superior Tecnico, Lisboa, Portugal, 2021.
31. Pragana, J.P.M.; Sampaio, R.F.V.; Bragança, I.M.F.; Silva, C.M.A.; Martins, P.A.F. Hybrid metal additive manufacturing: A state-of-the-art review. *Adv. Ind. Manuf. Eng.* **2021**, *2*, 100032. [CrossRef]
32. Pham, D.T.; Gault, R.S. A comparison of rapid prototyping technologies. *Int. J. Mach. Tools Manuf.* **1998**, *38*, 1257–1287. [CrossRef]
33. Karunakaran, K.; Suryakumar, S.; Pushpa, V.; Akula, S. Low cost integration of additive and subtractive processes for hybrid layered manufacturing. *Robot. Comput.-Integr. Manuf.* **2010**, *26*, 490–499. [CrossRef]
34. Yong-Taeg, O.; Fujino, S.; Morinaga, K. Fabrication of transparent silica glass by powder sintering. *Sci. Technol. Adv. Mater.* **2002**, *3*, 297–301. [CrossRef]
35. Yang, D.; Zhang, Y.; Song, X.; Chen, Y.; Shen, Z.; Yang, C. Effects of sintering temperature and holding time on porosity and shrinkage of glass tubes. *Ceram. Int.* **2016**, *42*, 5906–5910. [CrossRef]
36. Gualberto, H.R.; Lopes, R.S.; Da Silva, F.A.N.G.; Schnurr, E.; Junior, E.P.; De Andrade, M.C. Influence of Sintering Temperature on Mechanical Properties of Glass-Ceramics Produced with Windshield Waste. *Int. J. Chem. Eng.* **2019**, *2019*, 2531027. [CrossRef]
37. *ASTM C158-02*; Standard Test Methods for Strength of Glass by Flexure (Determination of Modulus of Rupture). ASTM: West Conshohocken, PA, USA, 2017.
38. Blasqem. Micro Esferas de Vidro. Available online: https://www.blasqem.pt/micro-esferas-vidro.php (accessed on 8 December 2022).
39. Coniex. Granalhas e Abrasivos. Available online: https://coniex.pt/pt/catalogo/go/tratamento-superficies-granalhagem-granalhas-abrasivos-aco-inox-micro-esfera-vidro-corindao-oxido-aluminio (accessed on 8 December 2022).
40. Jaafar, S.; Zaid, M.; Matori, K.; Ghazali, M.; Shofri, M.; Hisham, N.; Saparudin, D. Effect of sintering temperatures and foaming agent content to the physical and structural properties of wollastonite based foam glass-ceramics. *Sci. Sinter.* **2020**, *52*, 269–281. [CrossRef]